POSITRON ANNIHILATION CHARACTERIZATION OF NANOSTRUCTURED FERRITIC ALLOYS—M. J. Alinger and G. R. Odette (University of California, Santa Barbara), S. C. Glade and B. D. Wirth (University of California, Berkeley), Y. Nagai and M. Hasegawa (Tohoku University, Sendai Japan)

OBJECTIVE

The objective of this research was to probe nm-scale precipitates as well as the defect structure of nanostructured ferritic alloys (NFAs) using positron annihilation spectroscopy to provide further understanding of microstructure development during processing.

SUMMARY

Positron annihilation spectroscopy lifetime and orbital electron momentum spectroscopy (OEMS) data are in qualitative agreement with small angle neutron scattering (SANS) observations for NCs in NFAs. In the U14WT alloys, which do not contain yttrium, the positrons primarily annihilate in the matrix and matrix features like dislocations or small solute clusters. A small fraction of the positrons annihilate at large vacancy clusters or gas bubbles. In the case of the Y containing alloy, U14YWT, up to ≈50% of the positrons annihilate at non-magnetic features characteristic of Y-Ti-O NCs and, perhaps, smaller vacancy cluster-bubble type features.

PROGRESS AND STATUS

Introduction

Structural alloys used in the intense neutron fields of first wall and blanket structures of fusion reactors must minimize residual radioactivity arising from nuclear reactions as well as provide long-term stability of both the microstructure and mechanical properties. Microstructural stability includes the ability to successfully manage high levels of both transmutation products like helium and displacement of atoms from their lattice positions, creating excess concentrations of vacancies and self-interstitial atoms. In combination, these requirements present a unique material challenge within a materials science based approach to advanced alloy design and development [1,2,3,4,5].

A significant effort has been devoted to achieving high creep strength, radiation damage resistant alloys by creating a very high number density of fine-scale features that act as dislocation obstacles, serve as the dominant nucleation site for small helium bubbles and promote vacancy-interstitial recombination. Such fine-scale features have been observed in alloys traditionally classified as oxide dispersion strengthened (ODS) alloys. The aim of ODS alloys is to create a fine dispersion of oxide particles for enhanced creep strength. Traditionally it was believed that oxide particles are refined and homogeneously dispersed throughout the microstructure through mechanical alloying (MA) [6]. The MA powders are then consolidated using techniques such as hot extrusion and hot isostatic pressing (HIPing). However, it has recently been shown that, for specific alloy chemistries and processing routes, a high number density of coherent, nm-scale Y-Ti-O nanoclusters (NCs) can be produced by MA of Fe-Cr-Ti powders with Y_2O_3 followed by precipitation of Y, Ti, and O from solid solution during hot consolidation [7,8,9,10]. Such alloys have been described as nano-dispersion-strengthened ferritic alloys (NFAs).

In this study, positron annihilation lifetime spectroscopy (PALS) is used to detect open volume regions in NFAs. The chemical identity of the elements at the annihilation sites was also assessed by measuring the coincident Doppler broadening of the annihilation photons, referred to as orbital electron momentum spectroscopy (OEMS) [11]. In addition to probing open volume regions, positrons will preferentially localize, or ‘trap,’ in regions of stronger affinity. In contrast, elements or phases with a lower affinity tend to repel positrons. Through the use of these techniques, quantitative (or semi-quantitative) information on precipitate evolution, akin to results for age hardenable alloys, can be obtained [12].

Experimental Procedure

Materials

Gas atomized master alloy powders containing ≈14-wt% Cr, 0.4-wt% Ti and 3-wt% W were MA with and without 0.25-wt% Y_2O_3 by SPEX ball milling in argon for 8 hours. The milled powders were then degassed at 200°C for 24 hours, canned in seamless low carbon steel tubes and consolidated by hot isostatic pressing (HIPing) at 200 MPa for 3 h at 850, 1000, and 1150°C. The alloy codes used in this investigation are U14YWT (Fe-14Cr-3W-0.4Ti-0.25Y_2O_3) for alloys containing Y_2O_3 and U14WT without Y_2O_3 (Fe-14Cr-3W-0.4Ti). Additional details can be found in Ref. [13].

Small Angle Neutron Scattering (SANS)

Small angle neutron scattering (SANS) was performed on the 8 m SANS instrument (NG1) at the National Institute of Standards and Technology. With a neutron wavelength of 0.5 nm, the instrumental configuration yielded a maximum scattering vector, q ≈3.0 nm^{-1}. A strong ≈1.7 T magnetic field applied in the horizontal direction permitted measurement of both nuclear, $d\Sigma/d\Omega(q)_n$, and magnetic, $d\Sigma/d\Omega(q)_m$, neutron scattering cross sections, where:

$$\frac{d\Sigma}{d\Omega}(q,\phi) = \frac{d\Sigma}{d\Omega}(q)_n + \sin^2\phi \frac{d\Sigma}{d\Omega}(q)_m \qquad (1)$$

Here ϕ is the angle with respect to the magnetic field direction. Subtraction of parasitic background counts and normalization of the sample counts, transmissions and masses to a water standard were carried out to measure the absolute $d\Sigma/d\Omega(q,\phi)$. These absolute cross-sections were averaged over specified detector q and ϕ ranges, typically at ϕ = 0±30, 45±15, and 80±10, and used to evaluate the magnetic-to-nuclear scattering ratio (M/N). Note that the M/N is typically determined from scattering over the entire detector.

The scattering cross sections for the nanometer features associated with the variable of interest, $d\Sigma/d\Omega_f$, were determined by subtracting the control cross section (see reference 14 for a detailed description of the SANS data reduction and analysis procedures). For example, subtracting the $d\Sigma/d\Omega$ for U14WT from that for U14YWT was used to assess the effect of Y_2O_3. The $d\Sigma/d\Omega(q,\phi)$ specify the average size (<r>), size distribution ($\Delta r/r$), volume fraction (f) and number density (N) of scattering features. For features with a specified size (r):

$$\frac{d\Sigma}{d\Omega}_{mag}(q) = NV^2\left(\rho_f^{mag} - \rho_m^{mag}\right)^2 S(qr) \qquad (2)$$

Here, ρ_f^{mag} and ρ_m^{mag} are the feature and matrix magnetic coherent scattering length densities and S(qr) is a form factor that depends on the features shape and size [15]. We determined <r>, f, and N by fitting computed $d\Sigma/d\Omega(q)_m$ curves to the $d\Sigma/d\Omega(q)$ data assuming a log-normal distribution, parameterized by mode radius, r_m, $\Delta r/r$, and $d\Sigma/d\Omega(0)_m$ [14]. However, measuring f and N requires *knowledge* of the ρ_f and ρ_m. This is possible for magnetically saturated ferromagnetic alloys, where the matrix magnetic coherent scattering length density, ρ_m^{mag}, is known from the magnetic moment of the alloy (in this case accounting for Cr and other solutes) [16]. Assuming the features are primarily Y, Ti, and O, and non-magnetic, $\rho_f^{mag} \approx 0$.

Positron Annihilation Spectroscopy (PAS)

Positron Annihilation Spectroscopy (PAS) is a useful complementary tool for characterizing NCs and other key components of NFA microstructures. In a pure defect free crystal, positrons migrate by thermal

diffusion until they annihilate with an electron in the crystal. The annihilation occurs over a characteristic mean lifetime, which varies from element to element and is approximately 110 ps in pure iron [17].

However, during diffusion, positrons are trapped by various open-volume defects such as vacancy clusters, dislocations, and different types of interfaces. Additionally, positrons localize ('trap') within clusters of elements (or compound phases) that have a higher positron affinity than that of the matrix. The positron affinities for the most pertinent elements in NFAs are: Fe=-3.84, Cr=-2.62, Y=-5.31, W=-1.31, and Ti=-4.06, in units of eV [18]. The affinity differences essentially represent the trapping energy for a positron. Thus, for example, a positron would be trapped in a pure Y phase in an iron matrix with a binding energy of about 1.5 eV. While both Y and Ti will trap positrons, the affinity for O is not known, nor is it well established for the nanoclusters.

If the electron density is lower at a trapping site, the positron lifetime will increase relative to the lifetime in a defect-free bulk. Further, well-defined open-volume trapping features have a unique characteristic lifetime. For example in Fe, the lifetime associated with a dislocation is about 140 to 160 ps and a single vacancy 175 to 185 ps [19,20,21]. Positrons are strongly trapped in vacancy clusters and the lifetime initially increases rapidly with cluster size but saturates at ≈500 ps for clusters with more than ≈60 vacancies [22,23]. It is also known that positron lifetimes are longer in some insulating oxide compounds, which may form positronium with characteristic annihilation lifetimes that may exceed 1000 ps. The lifetime of Al_2O_3 is 150 ps [24] and in TiO_2 is 180 ps [25], but to our knowledge, is not known for the other oxides of interest.

The overall positron lifetime spectrum obtained for a situation where positron trapping and annihilation occurs at two defects as well as annihilation in the bulk material (3 lifetime components) is [26]:

$$D(t) = I_1 \exp\left(\frac{-t}{\tau_1}\right) + I_2 \exp\left(\frac{-t}{\tau_2}\right) + I_3 \exp\left(\frac{-t}{\tau_3}\right) \tag{3}$$

where t is time, I_1, I_2, and I_3 are the relative intensities of the three life time components τ_1, τ_2, and τ_3 and [17]:

$$\begin{aligned} \tau_1 &= \frac{1}{\lambda_b + \kappa_{d1} + \kappa_{d2}} \\ \tau_2 &= \frac{1}{\lambda_{d1}} \\ \tau_3 &= \frac{1}{\lambda_{d2}} \end{aligned} \tag{4}$$

where κ_{d1} and κ_{d2} are the trapping rates of the shorter and longer lifetime defects, respectively. λ_b, λ_{d1}, and λ_{d2} are the positron annihilation rates in the bulk material and defects, respectively. In turn, the relative intensities are:

$$\begin{aligned} I_1 &= 1 - I_2 - I_3 \\ I_2 &= \frac{\kappa_{d1}}{\lambda_b - \lambda_{d1} + \kappa_{d1} + \kappa_{d2}} \\ I_3 &= \frac{\kappa_{d2}}{\lambda_b - \lambda_{d2} + \kappa_{d1} + \kappa_{d2}} \end{aligned} \tag{5}$$

The trapping rates can be evaluated through the expression:

$$\kappa_i = \mu_i N_i \tag{6}$$

where μ_i is the trapping coefficient and N_i is the concentration of trapping sites (number density). In reality, a distribution of positron lifetimes reflecting a competition between a number of different trapping sites exist and the measured positron lifetime distribution reflects the competition between the dominant traps.

The two or three lifetime positron trapping model requires one additional assumption, namely the 'trapping regime.' Positrons can be trapped in either the diffusion or transition limited regimes, or a combination of both. Positron localization at trapping sites is complex and not well understood and it is possible that, in some cases, positron transition to a trapped state governs over diffusion trapping. The diffusion limited regime assumes that the probability of the positron diffusing to a trap prior to annihilation in the bulk governs positron behavior. In this case, the trapping coefficients for spherical traps (μ_{sphere}) and dislocations ($\mu_{\perp}$) are:

$$\mu_{sphere} = 4\pi r D_{+}$$
$$\mu_{\perp} = \frac{\rho_{\perp} D_{+}}{N} \qquad (7)$$

where r is the radius of the precipitate, $\rho_{\perp}$ is the dislocation density, D_{+} is the diffusivity of the positron (~2 cm^2s^{-1} in Fe-14Cr), and N is the effective number density which cancels out in Equation 6 for trapping at a dislocation. For the NFA materials in this investigation, the precipitate r and N have been obtained by SANS measurements. In a perfect crystal, all of the positron annihilation occurs in the matrix. However, at sufficient sink densities the lifetime of the positron in the trapping site(s) becomes a significant (measurable) fraction of the total annihilation events. Thus, positron lifetime analysis can provide information on the character, size, and number density of the trapping site(s).

Another feature of the annihilation process that can be exploited is the fact that momentum is conserved during the event that converts the positron-electron pair to two photons moving in approximately opposite directions. While the thermal positron itself has little momentum, that of the orbital electrons is much larger and varies both within a particular element (e.g., valence versus core electrons) and between elements. Thus, the distribution of momentum carries information about the chemistry of the annihilation site. By measuring both annihilation photons in coincidence, very high resolution measurements of the linear momentum of the electron-positron pair can be obtained, which provides the orbital electron momentum spectra (OEMS) (often called coincidence Doppler broadening, CDB spectroscopy). Typically, OEMS data are presented as the ratio of the amplitude of the photon counts [$I(p_L)$] at a particular value of momentum, p_L, to that for a reference material, in this case Fe. A common unit of p_L is the electron rest mass (m_o) multiplied by the speed of light (c). Each element or defect trapping feature has a characteristic [$I(p_L)$] normalized shape. For example vacancy clusters have a high intensity $I(p_L)$ at low momentum $p_L \approx 0$ while the $I(p_L)$ is lower at intermediate p_L compared with Fe. In an actual material $I(p_L)$ is determined by the weighted combination of individual annihilation sites.

The OEMS was measured using an experimental setup in which positrons emitted from a radioactive ^{22}Na source are confined and transported to the sample using a strong magnetic field (~1.0 kG). By reversing the orientation of the magnetic field (e.g., from up to down in a vertical direction), the positrons are still transported to the sample, but the majority and minority electron populations in a magnetic material is reversed. This enables spin-polarized, magnetic positron annihilation measurements [27], yielding data on the magnetic character of the positron annihilation site. When the normalized fraction of positron annihilations with high-momentum electrons versus low-momentum electrons is plotted for each magnetic field orientation, magnetic character of the positron annihilation site is revealed as a splitting of the two data points. In contrast, the data points and OEMS spectra are unchanged (superimposed) for positron annihilation in non-magnetic materials. This technique has been successfully used to confirm the non-magnetic behavior of embedded, nanometer-sized copper-rich precipitates in irradiated reactor pressure vessel steels [27] and has also been used in this investigation.

Results

The SANS results are summarized in Fig. 1 and are discussed in detail elsewhere for the HIP consolidated U14YWT alloys [28]. With increasing HIP consolidation temperature from 850 to 1150°C, the mean radius (r) increases from 1.25 to 1.71 nm, the volume fraction (f) decreases from 2.15 to 0.65%, and the number density (N) decreases from 2.57 to 0.30 x10^{24} m^{-3}.

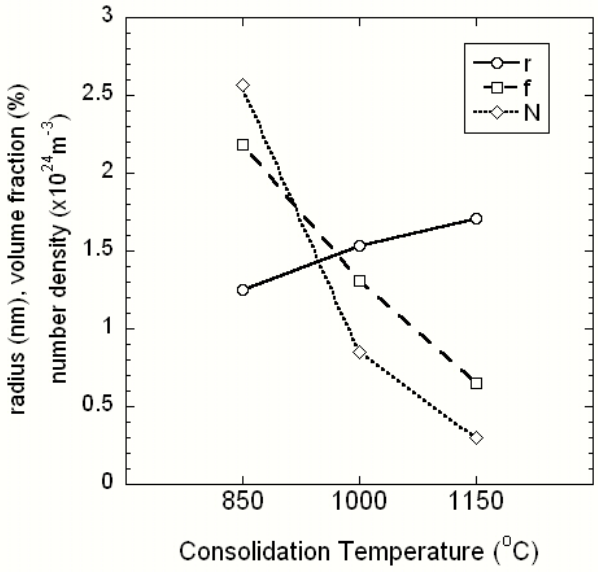

Fig. 1. Results of SANS data analysis for radius (r), volume fraction (f), number density (N), and magnetic to nuclear scattering ratio (M/N).

Positron OEMS

Fig. 2 shows the measured I(p_L) curves characteristic of Y_2O_3, Ti_2O_3, and TiO_2, normalized by dividing with the I(p_L) for unalloyed Fe providing characteristic annihilation momentum signatures for positrons which (might) trap in oxides embedded in the Fe matrix. The curves for the three oxides are generally similar with a substantial dip at intermediate p_L ≈5-30 (m_oc); Y_2O_3 has the deepest minimum.

Fig. 3 shows the corresponding normalized I(p_L)curves for U14WT (filled symbols) and U14YWT (open symbols) for HIPing at 850, 1000, and 1150°C. The I(p_L) dips for all of the HIPed alloys, except U14WT1150, at intermediate p_L with much larger decreases for the Y-containing alloys. The spectra, especially for U14YWT are qualitatively similar to, but weaker, than those for the pure oxides. With the exception of U14WT HIPed at 1150°C, all the alloys also show an I(p_L) peak at low p_L, indicative of open volume vacancy-bubble annihilation or, perhaps, an oxide type feature. The U14WT alloy HIPed at 1150°C shows the least evidence of annihilation in a Ti-O rich phase. Indeed in this case, the predominant annihilation is in the Fe-Cr-W-Ti matrix showing the effects of solutes or small solute clusters. The corresponding I(p_L) curves for Ti and Cr are shown in Fig. 4.

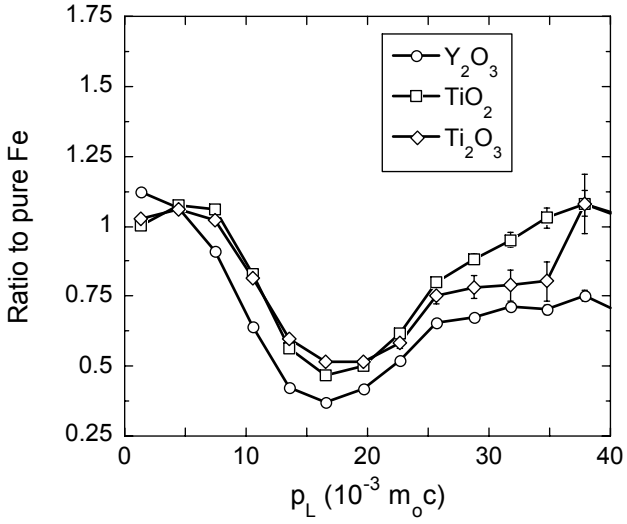

Fig. 2. Measured $I(p_L)$ curves characteristic of oxides Y_2O_3, Ti_2O_3, and TiO_2 normalized by dividing with the $I(p_L)$ for unalloyed Fe.

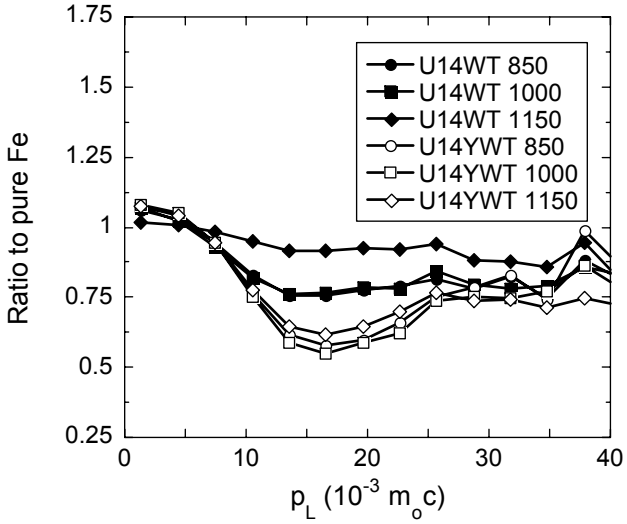

Fig. 3. PAS OEMS plot normalized to Fe.

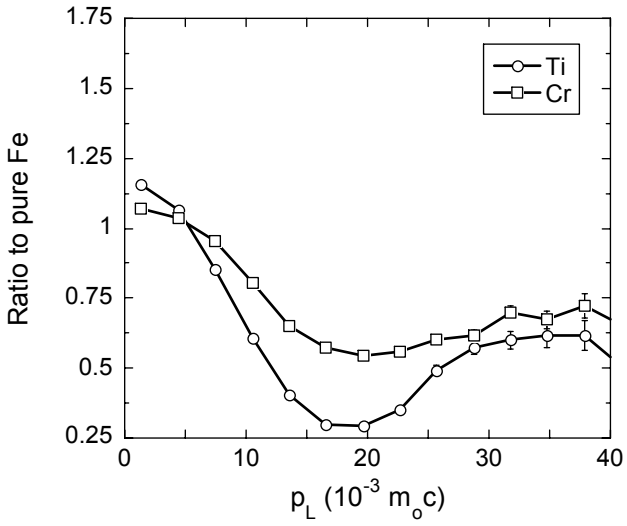

Fig. 4. I(p_L) curves for Ti and Cr.

The I(p_L) curves for the alloys containing both Ti and Y (U14YWT) are appreciably deeper than for those with only Ti (U14WT), and the depths increase at the lower HIPing temperatures. The deeper dips in the U14YWT versus U14WT alloys, as well as the trend with HIPing temperature, are consistent with an increasing trap sink strength for NC (U14YWT) and vacancy-bubble clusters and Ti-oxides (U14WT). Overall, the I(p_L) curves are consistent with a mixed set of annihilation sites in the matrix, likely to include NCs, vacancy clusters, and dislocations.

It is common to plot the OEMS data in terms of the relative fractions of high (W) versus low momentum (S) annihilations. The S and W parameters are determined by integrating the I(p_L) curves between specified p_L limits and dividing by the corresponding integration over the entire p_L range. The limits used in this work were 0.0 to 2.8 x$10^{-3}$$m_o$c (S) and 7.2 to 29.0 x$10^{-3}$$m_o$c (W), respectively, which is shown in Fig. 5.

Fig. 5 also shows the corresponding S-W points for various oxides and elemental Fe, Cr, and Ti. The W is lower and S is higher in the U14WT alloys compared to Fe, likely due to a combination of alloying effects and annihilation at vacancy clusters, or perhaps oxide-type features. However, from the relative positions on the S-W plot, the TiO and TiO_2 oxides themselves do not appear to be good candidates for the secondary annihilation sites. Indeed, the U14WT alloys fall along a tie line established in previous measurements between Fe and irradiated iron containing large vacancy clusters as well as Ti itself. The S-W position in the U14WT alloys is also consistent with annihilation at Ti clusters.

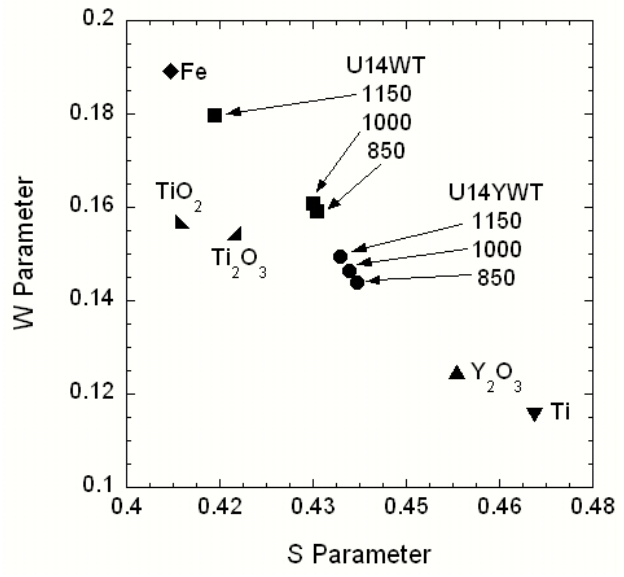

Fig. 5. PAS S-W analysis of the NFAs compared to several reference materials.

Fig. 6 is an expanded plot of Fig. 5 focusing on the U14WT and U14YWT alloys. The dashed lines connect the Fe data point to the measured values for the oxides (TiO_2, Ti_2O_3, and Y_2O_3) as well as Ti. The U14YWT alloys are shifted further to lower W and higher S and in the direction of Y_2O_3. The paired filled and unfilled symbols for each material represent the effects of magnetic polarization. Thus, there is a substantial splitting in ferromagnetic Fe and essentially no splitting in the oxides or paramagnetic Cr and Ti. The splitting is reduced to some extent in the U14WT alloys compared to Fe. However, the splitting is substantially reduced in the U14YWT alloys. This indicates a sizeable fraction of the annihilations take place in non-magnetic features.

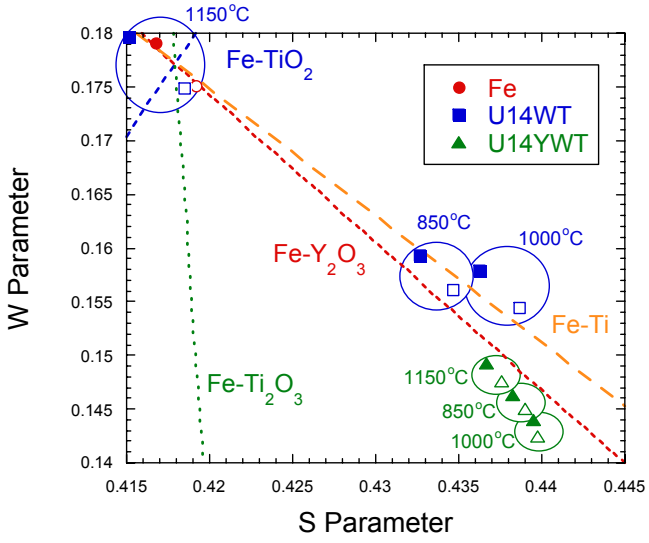

Fig. 6. Expanded plot of S-W analysis performed at LLNL with a line fit to Fe and Y_2O_3.

Positron Lifetime

The PAS lifetime data are shown in Fig. 7 and listed in Table 1. The right hand side of the lifetime plot shows the results of calculations for vacancy cluster and listed in lifetimes in iron [22]. In both alloys, short (τ_1) and long (τ_2) annihilation lifetimes are discernable. However, the lifetime in the U14WT alloys is dominated by a fraction I_1 of the annihilations in the matrix ≥85% with τ_1 ≈107 to 140 ps, reasonably characteristic with defect-free pure Fe (≈110 ps), and a fraction of annihilation at dislocations (≈140 ps) [29]. There is a small fraction of long lifetime annihilations (I_2 < 15%) with τ_2 ≈360 to 380 ps, characteristic of large vacancy clusters or gas bubbles; or even, perhaps, an oxide type feature. Notably, Schaefer and co-workers measured a similar long lifetime (360 ± 30 ps) component in nanocrystalline and nominally pure Fe with a mean grain size of 6 nm, but with a slightly larger intensity (≈33%) [20]. As well, Ohkubo and co-workers observe vacancy clusters with a lifetime of ≈340 ps in nominally pure Fe subject to high-speed deformation [30]. The predicted positron lifetime of vacancy clusters containing between 10 and 15 vacancies ranges from 330 to 380 ps [30]. The similarity of the lifetimes in the U14WT alloys and previous measurements on nanocrystalline iron indicate vacancy clusters as the likely positron trapping site. Notably, the fraction of τ_2 annihilations for U14YWT HIPed at 1150°C is only ≈4%.

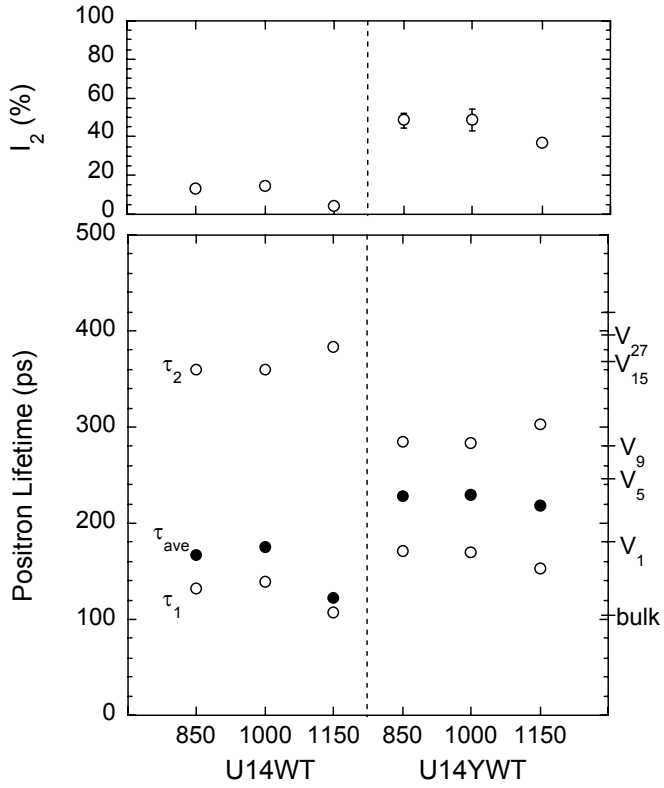

Fig. 7. PAS measured lifetimes and relative intensities for the controls and yttria containing alloys. The calculated lifetimes in Fe for V_x, where x is the number of vacancies in a cluster, are shown on the right axis [22].

Table 1. PAS lifetime data

Alloy	HIP Temp	τ_{av}	$\Delta\tau_{av}$	τ_1	$\Delta\tau_1$	τ_2	$\Delta\tau_2$	I_2	ΔI_2
	(°C)	(ps)	(ps)	(ps)	(ps)	(ps)	(ps)	(%)	(%)
U14WT	850	166.9	0.2	132.1	0.5	360.4	5.2	13.0	0.5
U14WT	1000	175.4	0.2	139.0	1.0	359.1	5.7	14.3	1.1
U14WT	1150	121.8	0.3	107.1	0.9	383.2	22.3	4.1	1.0
U14YWT	850	228.5	0.3	171.0	3.0	284.6	6.7	48.4	3.9
U14YWT	1000	229.5	0.2	169.6	4.6	283.1	5.3	48.6	5.3
U14YWT	1150	218.4	0.2	153.5	1.6	302.9	2.1	37.0	1.5

In contrast, the τ_1 annihilation lifetimes of 154 to 172 ps are longer in the case of the U14YWT alloys, consistent with a mixture of annihilation at dislocations (≈140–160 ps) and vacancies (≈175 ps). The longer τ_2 annihilation lifetimes are shorter than in U14WT, ranging from ≈280 to 300 ps, but represent a much higher I_2 fraction from ≈37 to 49% of the total. The τ_2 increases and the intensity-fraction decreases slightly for the 1150°C HIP. Note these trends are similar to those in the OEMS data and suggest that a large fraction of annihilations take place in Y-Ti-O rich NCs.

Discussion

The lifetime data can be analyzed using the simplified rate theory approach outlined above. The potential positron trapping sites considered in this investigation are vacancies, vacancy clusters, fine scale precipitates and dislocations.

U14WT Alloys

As discussed above, the alloys that did not contain Y had a minor long lifetime component, τ_2, as indicated by a small I_2. A majority of the positrons annihilated in the bulk material, however, some (≈5–15%) annihilated in open volume or low electron density traps. These alloys did not contain a significant density of nm-scale precipitates, but TEM showed that they had a high dislocation density and fine grain size [31]. The severe deformation resulting from mechanical alloying also produces a high non-equilibrium concentration of vacancies [32]. In addition, the gas atmosphere used during milling (typically Ar for iron alloys) can be incorporated into the powders and has been shown to precipitate in fine bubbles associated with precipitates [33].

The U14WT alloy HIPed at 1150°C had a short lifetime component equivalent to that of bulk iron and a small (I_2≈4%) long lifetime component corresponding to a vacancy cluster size of ≈22 vacancies. This leads to an estimated cluster density of 4.05×10^{20} m^{-3}. Assuming an average vacancy formation energy from the literature of 175 kJ/mole this prediction would yield a total vacancy concentration equal to that of the thermal equilibrium concentration in Fe at 1025°C [34].

For the alloys HIPed at 850 and 1000°C, the short lifetime components are longer than that of pure iron, but shorter than for a single vacancy. A lifetime value in this range is generally attributed to annihilation at a dislocation [19]. This data can be analyzed by assuming a high but not unreasonable value for MA materials, dislocation density (≈10^{15} m^{-2}), and with τ_2 produced by trapping at vacancy clusters-bubbles as seen in the alloy HIPed at 1150°C. From the positron lifetime, the cluster sizes for the 1000 and 850°C HIPed U14WT are both ≈15 vacancies. The resulting calculated densities of vacancy clusters are 3.8 and 3.4 $\times 10^{22}$ m^{-3} for 1000 and 850°C, respectively. These densities correspond approximately to the thermal equilibrium vacancy concentration expected at the melting point of iron.

U14YWT Alloys

In contrast, the τ_1 annihilation lifetimes (154 to 172 ps) are longer in the case of the U14YWT alloys. The τ_2 annihilation lifetimes are shorter than in U14WT, ranging from (280 to 300 ps), but represent a much higher I_2 fraction of the total. These trends are similar to those in the measured OEMS and suggest that a large fraction of annihilations take place in Y-Ti-O rich NCs.

Measured lifetimes for Al_2O_3 and TiO_2 are in the range of 150 to 180 ps, and it is unclear what lifetime to expect from the NC; especially considering that they are likely not fully formed oxides, may be complexed with vacancies and/or associated with dislocations. Fig. 8 shows the U14YWT OEMS curves normalized by the corresponding 'baseline' curve for the U14WT alloy HIPed at 1150°C, along with the corresponding curves for the oxides. The heavy dashed line in Fig. 8a is the Y_2O_3 data weighted by 0.45, corresponding to the average value of I_2 assuming that the NC annihilation component corresponds to the lifetime τ_2. The longer lifetime can be attributed to either a much longer lifetime in the Y_2O_3 than Al_2O_3 or TiO_2 or because of trapping in vacancy cluster-nanocluster complexes. Fig. 8b shows the results of using a Y_2O_3 weighting fraction of 0.65, obtained by fitting to the average U14YWT spectra at 850, 1000, and 1150°C, over the range of 10–40 x10^{-3} m_oc. Notably, the weighting fraction value of 0.65 corresponds most closely to the intensity values associated with τ_1 at a lifetime of 165 ps. This lifetime is within the expected regime from the other oxides.

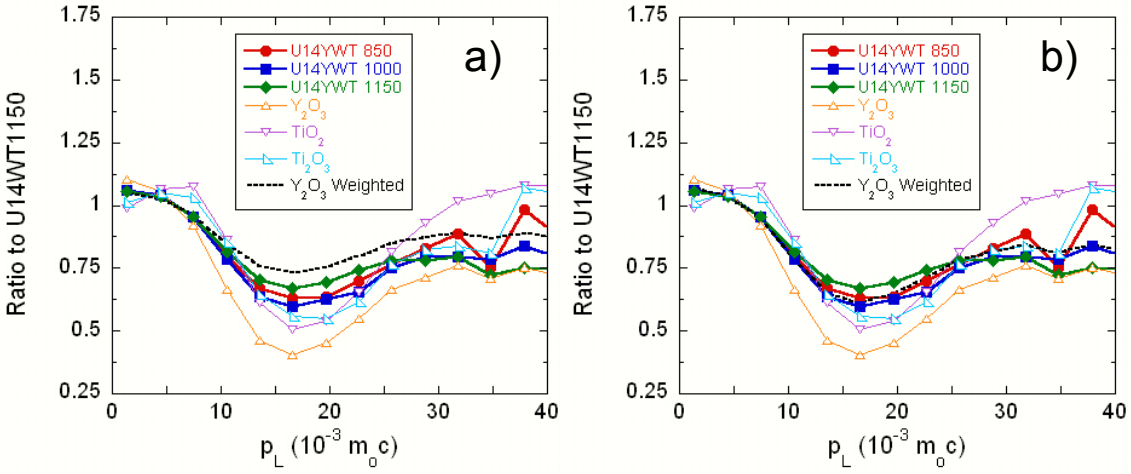

Fig. 8. I(p_L) curves for the U14YWT alloys for the 3 HIPing temperatures normalized by the corresponding 'baseline' curve for the U14WT alloy HIPed at 1150°C, along with the corresponding curves for the oxides. The heavy black dashed line is the Y_2O_3 weighted average and is 0.45 in Fig. a and 0.65 in Fig. b.

Thus, if we are to assume instead that τ_1 is due to annihilation at NCs, consistent with the analysis leading to Fig. 8b, then τ_2 is attributed to annihilation in vacancy clusters. In such a scenario, vacancy cluster sizes, estimated from the lifetime, would contain 9–10 vacancies, smaller than those in the U14WT. The required number density of such clusters, as calculated from the simplified trapping model are 1.1x10^{24}, 4.2x10^{24}, and 1.0x10^{25} m^{-3} for 1150, 1000, and 850°C, respectively. These vacancy concentrations are very high and appear to be somewhat unrealistic, though MA is capable of creating very high dislocation densities.

An alternate assumption is that the long lifetime component is associated with annihilation in nanoclusters (as in Fig. 8a), and the short lifetime component is at dislocations; a dislocation density of 1.1x10^{16} m^{-2} is estimated from the simplified trapping model for the U14YWT HIPed at 1150°C. At 1000 and 850 the

corresponding dislocation densities would be 1.7×10^{16} and 4.3×10^{16}, respectively. The high dislocation density from this analysis is problematic, but implies that the NCs are effective at pinning dislocations and inhibiting recovery with respect to the U14WT alloys without NCs. Note the vacancy clusters, present in the U14WT alloy, may also exist in the U14YWT alloy. However, the NC number densities are an order of magnitude greater and thus have a much larger effective positron sink strength.

Of course, the microstructure of these alloys is very complex, with multiple positron trapping sites, and this simplified analysis neglects consideration of the electronic structure of the nanoclusters, which is likely different than Y_2O_3. However, the results clearly show positron annihilation spectra consistent with Y-Ti-O and vacancy cluster lifetimes as well as with other nanocrystalline Fe and fast-deformation Fe [20,22]. Further clarification of the trapping sites in these alloys requires additional research.

Summary and Conclusions

In summary, the PAS lifetime and OEMS data are in qualitative agreement with the SANS observations. In the U14WT alloys, which do not contain Y, the positrons primarily annihilate in the matrix as well as features like dislocations or small solute clusters. A small fraction of the positrons annihilate at large vacancy clusters (or gas bubbles) that are also probably complexed with solutes. The simplified positron lifetime trapping (rate theory) analysis indicates high dislocation densities and vacancy concentrations are (reasonably) consistent with that anticipated in MA and HIPed alloys.

In the case of U14YWT alloys, which contained Y, up to $\approx$50% of the positrons annihilate at non-magnetic features associated with an S-W position indicating the presence of Y-Ti-O NCs and, perhaps, smaller vacancy cluster type features. Interpretation of the lifetime data for these alloys is difficult and depends on which positron lifetime is assumed to be associated with the NCs. Regardless, these alloys have a high concentration of defects, whether they are dislocations or vacancy clusters. Further investigation is required to better understand these relationships.

Future Work

Future work will focus on collecting and analyzing positron lifetime data for a series of thermally annealed MA957 specimens for which SANS data on the NC evolution exists as well as lifetime measurements for Y_2O_3. Also, we plan to perform Monte-Carlo simulations of the diffusion of positrons in alloys incorporating their effective trapping strength for the trapping limited regime as well as the effects of multiple positron trapping sites.

Acknowledgements

The authors gratefully acknowledge the supply of the Fe-14Cr powders and many helpful discussions with Dr. D. Hoelzer of ORNL. We also thank Doug Klingensmith (UCSB) for his contributions to the SANS experiments. We acknowledge the support of the National Institute of Standards and Technology, U.S. Department of Commerce, in providing facilities used in this work. This research was supported by DOE Office of Fusion Energy Science (Grant # DE-FG03-94ER54275) and the INERI DOE Office of Nuclear Energy through a subcontract with ORNL (Grant # 400014112).

References

[1] S. Yamashita, K. Oka, S. Ohnuki, N. Akasaka, and S. Ukai, Phase Stability of Oxide Dispersion-Strengthened Ferritic Steels in Neutron Irradiation, J. Nucl. Mater. 307–311 (2002) 283–288.
[2] J. Saito, T. Suda, S. Yamashita, S. Ohnuki, H. Takahashi, N. Akasaka, M. Nishida, and S. Ukai, Void Formation and Microstructural Development in Oxide Dispersion Strengthened Ferritic Steels During Electron-Irradiation, J. Nucl. Mater. 258–263 (1998) 1264–1268.

[3] K. Asano, Y. Kohno, A. Kohyama, T. Suzuki, and H. Kusanagi, Microstructural Evolution of an Oxide Dispersion Strengthened Steel under Charged Particle Irradiation, J. Nucl. Mater. 155–157 (1988) 928–934.
[4] H. Kinoshita, N. Akasaka, H. Takahashi, I. Shibahara, and S. Onose, Microstructural Change on Electron Irradiated Oxide Dispersion Strengthened Ferritic Steels, J. Nucl. Mater. 191–194 (1992) 874–878.
[5] V. V. Sagaradze, V. I. Shalaev, V. L. Arbuzov, B. N. Goshchitskii, Y. Tian, W. Qun, and S. Jiguang, Radiation Resistance and Thermal Creep of ODS Ferritic Steels, J. Nucl. Mater. 295 (2001) 265–272.
[6] J. S. Benjamin, Dispersion Strengthened Superalloys by Mechanical Alloying, Metall. Trans. (1970) 2943–2951.
[7] T. Okuda and M. Fujiwara, Dispersion Behavior of Oxide Particles in Mechanically Alloyed ODS Steel, J. Mater. Sci. Lett. 14 (1995) 1600–1603.
[8] S. Ukai, T. Nishida, and H. Okada, Development of Oxide Dispersion Strengthened Ferritic Steels for FBR Core Application, (I), J. Nucl. Sci. Technol. 34 (3) (1997) 256–263.
[9] S. Ukai, T. Nishida, T. Okuda, and T. Yoshitake, R&D of Oxide Dispersion Strengthened Ferritic Martensitic Steels for FBR, J. Nucl. Mater. 258–263 (1998) 1745–1749.
[10] M. J. Alinger, G. R. Odette, and D. T. Hoelzer, The Development and Stability of Y-Ti-O Nanoclusters in Mechanically Alloyed Fe-Cr Based Ferritic Alloys, J. Nucl. Mater. 329–333 (2004) 382.
[11] R. W. Siegel, Positron Annihilation Spectroscopy, Annu. Rev. Mater. Sci. 10 (1980) 393–425.
[12] A. Dupasquier, P. Folegati, N. de Diego, and A. Somoza, Current positron studies of structural modifications in age-hardenable metallic systems, J. Phys., Condens. Matter 10 (1998) 10409–10422.
[13] M. J. Alinger, On the Formation and Stability of Nanometer Scale Precipitates in Ferritic Alloys During Processing and High Temperature Service, Ph.D. Thesis, University of California, Santa Barbara (2004) 341.
[14] E. Mader, Ph.D. Thesis, University of California, Santa Barbara (1995).
[15] G. Kostorz, Treatise on Materials Science and Technology - Neutron Scattering, Vol. 15, New York: Academic Press (1979).
[16] ILL Neutron Data Booklet, A.-J. Dianoux and G. Lander (eds.), Institute Laue-Langevin (2001).
[17] T. E. M. Staab, R. Krause-Rehberg, and B. Kieback, Positron annihilation in fine-grained materials and fine powders -an application to the sintering of metal powders, J. Mater. Sci. 34 (1999) 3833–3851.
[18] M. J. Puska, P. Lanki, and R. M. Nieminen, Positron affinities for elemental metals, J. Phys.,: Condens. Matter (1989) 6081–6093.
[19] Y. Kamimura, T. Tsutsumi, and E. Kuramoto, Calculations of positron lifetimes in a jog and vacancies on an edge-dislocation line in Fe, Phy. Rev. B 52 (1995) 879–885.
[20] H.-E. Schaefer, R. Wurschum, R. Birringer, and H. Gleiter, Structure of nanometer-sized polycrystalline iron investigated by positron lifetime spectroscopy, Phy. Rev. B 38 (1988) 9545–9554.
[21] C. Hidalgo, G. Gonzalez-Doncel, S. Linderoth, and J. San Juan, Structure of dislocations in Al and Fe as studied by positron-annihilation spectroscopy, Phys. Rev. B 45 (1992) 7017–7021.
[22] H. Ohkubo, Z. Tang, Y. Nagai, M. Hasegawa, T. Tawara, and M. Kiritani, Positron annihilation study of vacancy-type defects in high-speed deformed Ni, Cu and Fe, Mater. Sci. Eng. A 350 (2003) 95–101.
[23] P. A. Sterne (personal communication 2004).
[24] M. Hasegawa, Y. Nagashima, K. Kawashima, T. Hyodo, S. Yamaguchi, M. Forster, and H.-E. Schaefer, Irradiation-induced voids in alumina single crystal studied by positron annihilation, Nucl. Instrum. Methods B 91 (1994) 263.
[25] Y. Nagai (personal communication 2004).
[26] R. Krause-Rehberg and H. S. Leipner, Positron Annihilation in Semiconductors, Springer, New York (1999).
[27] P. Asoka-Kumar, B. D. Wirth, P. A. Sterne, R. H. Howell, and G. R. Odette, Composition and magnetic character of nanometer-size Cu precipitates in reactor pressure vessel steels: Implications for nuclear power plant lifetime extension, Philos. Mag. Lett. 82 (2002) 609–615.
[28] M. J. Alinger, G. R. Odette, and D. T. Hoelzer, Processing Optimization for Nanocluster Formation in Nanostructured Ferritic Alloys, Metallurgical and Materials Transactions A (to be submitted).

[29] Y. K. Park, J. T. Waber, M. Meshii, C. L. Snead, and C. G. Park, Dislocation studies on deformed single crystals of high-purity iron using positron annihilation: Determination of dislocation densities, Phys.l Rev. B 34 (1986) 823–836.
[30] H. Ohkubo, Z. Tang, Y. Nagai, M. Hasegawa, T. Tawara, and M. Kiritani, Positron annihilation study of vacancy-type defects in high-speed deformed Ni, Cu and Fe, Mater. Sci. Eng. A 350 (2003) 95–101.
[31] H. Kishimoto, M. J. Alinger, G. R. Odette, and T. Yamamoto, TEM Examination of Microstructural Evolution During Processing of 14CrYWTi Nanostructured Ferritic Alloys, J. Nucl. Mater. 329–333 (2004) 369–371.
[32] H. H. Tian and M. Atzmon, Kinetics of Microstructure Evolution in Nanocrystalline Fe Powder During Mechanical Alloying, Acta Mater. 47 (1999) 1255–1261.
[33] M. Klimiankou, R. Lindau, and A. Moslang, Energy-filtered TEM imaging and EELS study of ODS particles and Argon-filled cavities in ferritic-martensitic steels, Micron 36 (2005) 1–8.
[34] H. Schultz, Defect parameters of b.c.c. metals: Group-specific trends, Mater. Sci. Eng. A 141 (1991) 149–167.